Efficient Electronic Excitation Transfer via Phonon-Assisted Dipole-Dipole Coupling in Fe^{2+}:Cr^{2+}:ZnSe

Günter Steinmeyer[1,2,*] Jens W. Tomm[1] Pia Fuertjes[1] Uwe Griebner[1] Stanislav S. Balabanov[3] and Thomas Elsaesser[1]

[1]*Max Born Institute for Nonlinear Optics and Short Pulse Spectroscopy, Max-Born-Straße 2a, Berlin 12489, Germany*

[2]*Physics Department, Humboldt University, Newtonstraße 15, Berlin 12489, Germany*

[3]*G.G. Devyatykh Institute of Chemistry of High-Purity Substances of the Russian Academy of Sciences, Tropinin Str. 49, Nizhny Novgorod 603951, Russia*

Cr^{2+} - and Fe^{2+} -doped ZnSe crystals are laser materials with phonon-broadened absorption and emission spectra, which provide broadband laser gain in the 2- to 5-μm wavelength range. While Cr^{2+}:ZnSe can be directly pumped with high-power Er, Ho, or Tm lasers, no such possibility exists for Fe^{2+}:ZnSe. To this end, electronic excitation transfer between Cr^{2+} and Fe^{2+} ions in codoped ZnSe is investigated as an alternative excitation process in photo luminescence (PL) experiments with sub-10-ns temporal resolution. For a wide range of ion concentrations, we observe nonexponential decays of Cr^{2+} PL on a microsecond time scale, a 60-ns rise time of Fe^{2+} PL at high doping densities, and a prolonged decay of Fe^{2+} PL due to the temporal characteristics of excitation transfer over a range of interionic distances. Using a multi-rate equation model, the transfer process is analyzed on length scales up to 30 nm and compared to the established continuum model approach. The analysis reveals an unexpectedly efficient excitation transfer from Cr^{2+} to Fe^{2+} ions with an enhancement of the excitation transfer rates by up to a factor of 5 in comparison to resonant dipole-dipole coupling. The enhancement is assigned to (multi)phonon-assisted excitation transfer, in analogy to the phonon-mediated efficient radiationless decay of the excited Fe^{2+} state. As nonradiative losses and excitation transfer show different temperature scaling, a cryogenic temperature regime is found that promises overall efficiencies above 50%, making Fe^{2+}:Cr^{2+}:ZnSe a much more viable alternative to parametric conversion schemes in the midinfrared range.

I. INTRODUCTION

Zinc selenide and related wide-band-gap II-VI materials represent useful host materials in which transition-metal ions such as Cr^{2+} or Fe^{2+} can act as active ion for solid-state lasers in the midinfrared (mid-IR). For this combination of laser host and active ion, efficient laser operation in different regimes (continuous-wave, Q-switched, gain-switched, mode-locked) has been demonstrated [1–4], and even commercial laser systems are available [5]. However, the latter currently only come with singly doped gain materials. In particular, there is additional interest in extending the emission wavelength range based on Cr^{2+} or Fe^{2+} active ions.

The emission wavelength of a specific ion can be manipulated by the choice of the binary host material, Zn and Cd chalcogenides, via the associated modification of the crystal field. This mechanism also leads to the use of ternary mixed-crystal hosts, such as Zn$_{1-x}$Mg$_x$Se [6–10], Cd$_{1-x}$Mn$_x$Te [11–13], Zn$_{1-x}$Cd$_x$Se, and ZnS$_{1-x}$Se$_x$ [14].

Another key goal is to design such light sources simpler and more affordable. One pertinent way is the codoping of laser crystals with two different ion types, enabling to pump one ion species with a simple and inexpensive pump laser. Provided there is energy transfer between the ions, this allows transfer of the population from one ion species to the other [15–17]. To this end, systems codoped with Tm and Ho are a proven combination in the 2-μm spectral range [18,19].

In the present study we address the less-explored Fe^{2+}:Cr^{2+}:ZnSe material system [18,20], where commercially available Tm-doped lasers can be utilized to excite Cr^{2+} ions at approximately 1.9 μm, yet exploit Fe^{2+} laser gain at approximately 4.1 μm. Fedorov *et al.* [16] and Antonov *et al.* [21] studied the Cr$^{2+} \rightarrow$ Fe^{2+} excitation transfer for very heavily doped samples ($n_{\mathrm{Cr,Fe}} \approx 2 \times 10^{19}$ cm^{-3}) and discussed relevant time constants. Recent time-resolved photo luminescence (PL) experiments in the midinfrared

have given insight into the buildup and decay of Fe^{2+} PL after excitation transfer from resonantly pumped Cr^{2+} ions [22]. It should be pointed out that Ref. [21] did not outline an overly optimistic perspective about the effective utility of the $Cr^{2+} \to Fe^{2+}$-excitation scheme for practical laser applications as the latter requires an accurate quantification of the microscopic processes involved.

The results presented in this paper address $Cr^{2+} \to Fe^{2+}$ excitation transfer through an in-depth comparison and analysis of both the luminescence intensities and kinetics of Cr^{2+}:ZnSe, Fe^{2+}ZnSe, and codoped Fe^{2+}:Cr^{2+}:ZnSe ($n_{Cr,Fe} \leq 6 \times 10^{18}$ cm^{-3}) crystals from different suppliers. Experimental kinetics are analyzed by model calculations. Our results allow for a separation of loss mechanisms and quantification of the dynamics in the $Cr^{2+} \to Fe^{2+}$ excitation transfer with a time resolution of better than 10 ns.

II. RESONANT EXCITATION TRANSFER: THE FÖRSTER MECHANISM

At sufficiently high doping levels, nonradiative dipole-dipole coupling can lead to a significant energy transfer from primarily excited donor ions to acceptor ions in the ZnSe host material (Fig. 1) [25–27]. For Fe^{2+}:Cr^{2+}:ZnSe, transfer from the Cr^{2+} donor to the Fe^{2+} acceptor offers an appealing alternative to direct excitation of Fe^{2+} as it enables the use of powerful Tm- or Ho-based pump sources, cf. Fig. 2(b). The rate W_{DA} of resonant transfer from an individual donor to an individual acceptor [16,28] separated by an interionic distance r follows an r^{-6} dependence:

$$W_{DA} = \frac{1}{\tau_{trans}} = \left(\frac{1}{4\pi\epsilon_0}\right)^2 \frac{3\pi\hbar e^4}{n^4 m_e^2 \omega^2} \frac{1}{r^6} f_D f_A$$

$$\times \int g_D(E) g_A(E) dE = \alpha_{DA} r^{-6}. \quad (1)$$

Here e and m_e are electron charge and mass, respectively. ϵ_0 is the vacuum permittivity, $\hbar = h/(2\pi)$ Planck's constant, n the refractive index of the host material. ω is chosen as the angular frequency at maximum overlap of the normalized spectral density functions g_D and g_A describing donor emission and acceptor absorption, cf. Fig. 2(c). f_D and f_A is the oscillator strength of the donor and the acceptor, respectively. Oscillator strengths are related to the respective cross sections $\sigma(\nu)$ [28] via

$$f = 4\pi\epsilon_0 \frac{m_e c}{\pi e^2} \int \sigma(\nu) d\nu, \quad (2)$$

where c is the speed of light and ν is the optical frequency.

Table I summarizes the different quantities required for calculation of the rates of resonant $Cr^{2+} \to Fe^{2+}$ excitation transfer. One derives a coefficient $\alpha_{DA} = 90$ nm^6/μs.
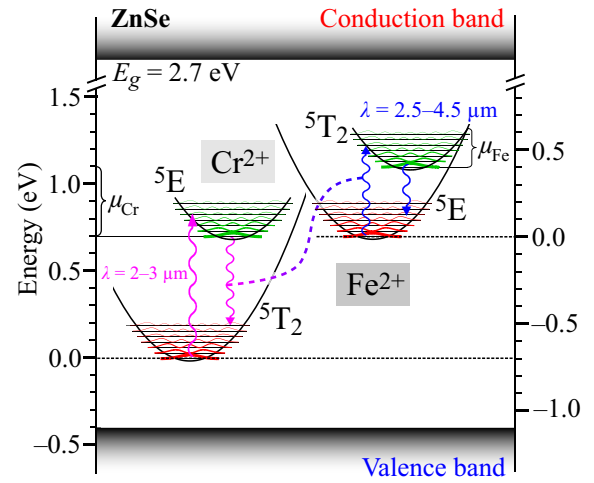

FIG. 1.   Schematic energy diagram of Fe^{2+} and Cr^{2+} in ZnSe according to Refs. [4,23]. μ_{Fe} and μ_{Cr} indicate the thermal activation energy according to the semiclassical model, cf. Table III. Vibronic substates are spaced by the LO phonon energy of 31 meV in ZnSe [24]. Resonant excitation transfer is indicated by the dashed curve.

Using the radiative lifetime τ_{Cr} of singly doped Cr^{2+}:ZnSe, one can derive a range parameter $R_0 = \sqrt[6]{\alpha\tau_{Cr}} = 2.8$ nm [28], which we refer to as the Förster radius in the following. In turn, this leads to a critical doping density $n_0 = 3/(4\pi R_0^3) = 1.1 \times 10^{19}$ cm^{-3}. It is worthwhile to note that such quantities account for resonant excitation transfer exclusively, i.e., for photon energies in the range where the Cr^{2+} emission and the Fe^{2+} absorption spectrum overlap. The overlap region covers a minor fraction of the Cr^{2+} emission and Fe^{2+} absorption spectra, resulting in a value of the overlap integral of 1.17 eV^{-1}. For perfect overlap, i.e., a negligible spectral shift between the two spectra, the integral would reach the substantially higher value of 4.2 eV^{-1}. On top of the resonant transfer described by W_{DA}, there is nonresonant phonon-assisted excitation transfer from Cr^{2+} to Fe^{2+} ions, which is discussed in Sec. VII below.

III. EXPERIMENTAL METHODS

Samples belonging to three groups, Cr^{2+}:ZnSe, Fe^{2+}:ZnSe, and codoped Fe^{2+}:Cr^{2+}:ZnSe, are acquired from Egorov Scientific USA, 3photon Lithuania, and IPG Photonics USA. In addition, home-grown samples are studied. The latter are obtained by diffusion doping a chromium film into high-purity chemical-vapor deposited (CVD) ZnSe at a temperature of about 1100 °C and an argon pressure of 100 MPa [32]. To denominate the different samples, we use the designations Cr*nn*Fe*mm*, with *nn* × 10^{17} cm^{-3} = n_{Cr} and *mm* × 10^{17} cm^{-3} = n_{Fe} describing the different ion concentrations (Table II). As ion concentrations in our samples do not exceed 10^{19} cm^{-3}, we expect
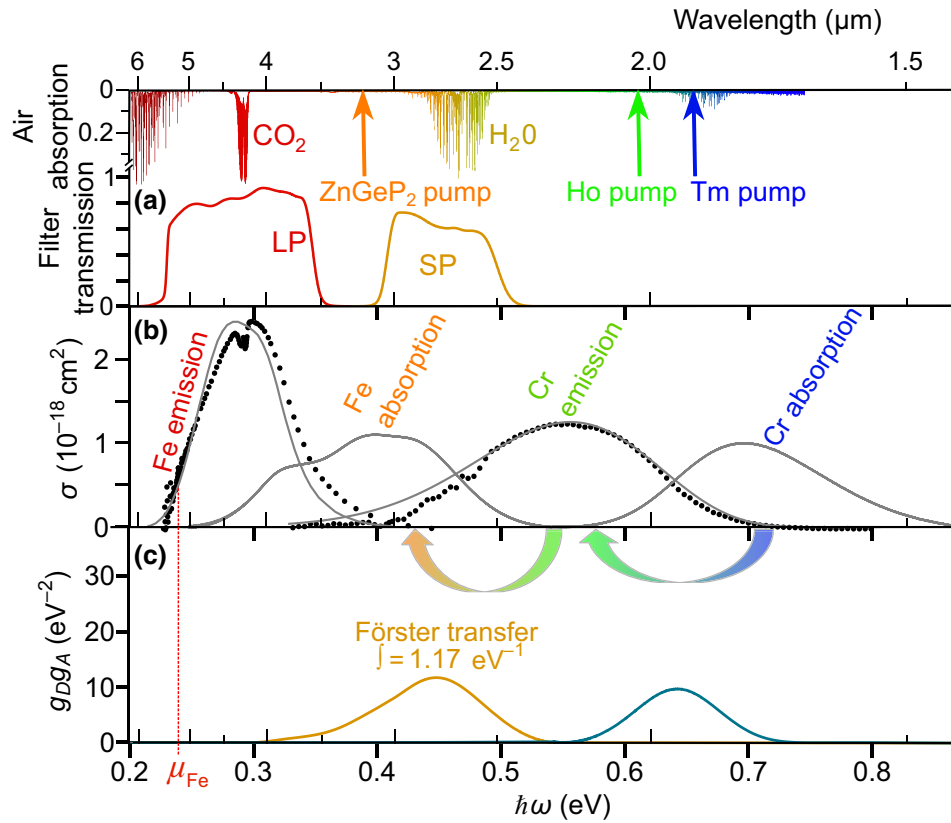
FIG. 2. (a) Air absorption in the setup used and transmission of the filter sets (spectral windows). LP, long-pass filter; SP, short-pass filter. Arrows indicate excitation wavelengths used in the experiments. (b) Absorption and emission cross sections of the Cr^{2+} and Fe^{2+} ions measured at room temperature. Symbols: measured data. Gray curves: fits used to extrapolate over regions of strong atmospheric absorptions. The emission cross section of the Fe^{2+} ions is taken from Ref. [25] and is measured at liquid nitrogen (LN_2) temperatures; all other curves are based on our own measurements. μ_{Fe} indicates the excitation energies of the Fe^{2+} ion. (c) Spectral overlaps of Cr^{2+} and Fe^{2+} ions.

the practical absence of reabsorption effects as is indicated by calculating donor-donor and acceptor-acceptor transfer rates with Eq. (1). All samples are polished

TABLE I. Quantities required [29–31] for computing transfer rates for the Förster excitation transfer via Eq. (1) and resulting Förster radius R_0 and critical doping density n_0. Overlap factors $\int g_D(E)g_A(E)dE$ are computed from our own measurements.

Quantity	DA $Cr^{2+} \to Fe^{2+}$
n	2.442
max. $\sigma_{em}^{Cr}(10^{-18} \text{ cm}^2)$	1.25
max. $\sigma_{abs}^{Fe}(10^{-18} \text{ cm}^2)$	1.0
f_D	2.2×10^{-3}
f_A	1.4×10^{-3}
$\hbar\omega$ (eV)	0.45
$\int g_D(E)g_A(E)dE$ (eV^{-1})	1.17
α_{DA} (nm^6/µs)	90
$\tau_{trans}(a/\sqrt{2})$ (ps)	48
R_0 (nm)	2.8
n_0 (10^{18} cm^{-3})	11

to optical grade, as required for gain elements in lasers.

The samples are characterized by standard transmission measurements at ambient temperature ($T = 300$ K). Concentrations of optically active Cr^{2+} and Fe^{2+} ions as given in Table II are determined using the commonly accepted peak absorption cross section of 1.1×10^{-18} cm^2 and 0.97×10^{-18} cm^2 for Cr^{2+} and Fe^{2+} ions, respectively [13,16,33]. To detect trace amounts of Fe^{2+} ions in the Cr^{2+}-doped samples, the transmittance at a sample temperature of $T = 10$ K is measured on the $^5E \to ^5T_2$ transition, cf. Fig. 1. This transition (among others) gives rise to two distinct lines, $\gamma_1 \to \Gamma_5$ and $\gamma_4 \to \Gamma_5$ [34,35], at wavelengths of 3.654 and 3.675 µm, respectively. The Fe^{2+}-detection limit corresponds to a concentration of 3×10^{16} cm^{-3}. Table II indicates Fe^{2+} content at the detection limit for one of the nominally singly Cr^{2+}-doped samples whereas $n_{Fe} > 5 \times 10^{17}$ cm^{-3} for all codoped samples.

Steady-state PL measurements are performed with a Bruker IFS66v Fourier transform spectrometer incorporating a (Hg, Cd)Te mid-IR detector. The samples are excited at a wavelength of $\lambda_{ex} = 1.91$ µm by a continuous-wave

TABLE II.　Overview of the three sample groups of ZnSe crystals. CVD, chemical vapor deposition; n_{Cr}, n_{Fe}, doping densities.

	Crystal	Remark	Single crystalline	$n_{Cr}(10^{18} \text{ cm}^{-3})$	$n_{Fe}(10^{18} \text{ cm}^{-3})$
Fe^{2+}-doped	Fe40	Random oriented	+		4
Cr^{2+}-doped	Cr10	CVD/diffused [32]	-	1	
	Cr27	CVD/diffused [32]	-	2.7	0.03
	Cr28	CVD/diffused [32]	-	2.8	
	Cr55	CVD/diffused [5]	-	5.5	
Codoped	Cr07Fe08	Bridgman/diffused	+	0.68	0.8
	Cr20Fe20a	(110) oriented	+	2	2
	Cr20Fe20b	Bridgman/diffused	+	2	2
	Cr42Fe05	Bridgman/diffused	+	4.2	0.5
	Cr67Fe61	CVD/diffused [5]	-	6.7	6.1
	Cr65Fe75	CVD/diffused [5]	-	6.5	7.5

Tm fiber laser. The signal-to-background ratio is as high as 370 for PL from the Cr^{2+} ions in the wavelength range between 2 and 3 μm. Absolute intensities of Cr^{2+} PL are compared between pristine cleaved and polished surfaces of selected crystals as well as between samples of different thicknesses prepared from the same crystal. For $\lambda_{ex} =$ 1.91 μm, none of the codoped samples show a clear PL signal attributable to Fe^{2+} emission. These findings contrast the low-temperature measurements of Antonov *et al.* [21] and Wang *et al.* [20]. Absorption and emission spectra are summarized in Fig. 2(b). We note that the intensity of ZnSe interband PL in the visible spectral range is a factor of 2 higher in the single-crystal compared to the CVD-grown samples at $T = 300$ K.

In the transient PL measurements, the samples are excited by pulses from a mid-IR optical parametric chirped pulse amplification system operating at a 1-kHz repetition rate. This system comprises a Ho:YLF regenerative amplifier as the pump, delivering pulses at 2.05 μm [spectral width (FWHM) 2 nm] with a 3-ps duration, and a $ZnGeP_2$ based optical parametric amplifier delivering signal pulses at 3.24 μm (spectral width 0.15 μm) with a 1-ps duration [36]. The average excitation power is set to 35 mW (18 mJ/cm^2) for both wavelengths. PL is detected with an InSb photodiode (Infrared Acc. ID413) with a buildup and decay time of 7 ns (1/e-decay at 50Ω), determining the time resolution of the experiment. Using a Femto DHPCA-100 amplifier with 1-kV/A transimpedance, this temporal resolution is almost preserved, i.e., we can specify a temporal resolution of better than 10 ns. A 4-GHz oscilloscope Tektronix DPO 70404C served for data recording. In multiple measurements, we find that the setup ensures a reproducibility of PL intensities of better than ±10% (standard deviation).

PL kinetics are measured with spectrally integrating detection in the range of the Cr^{2+} and the Fe^{2+} luminescence. The transmission characteristics of the spectral filters (Spectrogon, Edmund Optics) are plotted in Fig. 2(a). In detail, the transmission function is determined on its

high energy side by three long-pass filters that suppress the excitation laser wavelength $\lambda_{ex} = 2.05$ μm with an absorbance of more than OD = 10. In the long wavelength range, the decreasing sensitivity of the InSb detector cuts off the detection window. The spectral windows named SP (short pass) and LP (long pass) are defined by additional IR filter sets.

IV. TRANSIENT PHOTOLUMINESCENCE MEASUREMENTS

Time-resolved PL measurements are performed with resonant excitation of the samples, i.e., the Cr^{2+} doped as well as the codoped samples are excited at $\lambda_{ex} = 2.05$ μm, the Fe^{2+}-doped samples at $\lambda_{ex} = 3.24$ μm wavelength. We estimate that we directly excite a fraction $\mathcal{N}_{Cr} = N_{init}^{(Cr)}/n_{Cr} = 4.3\%$ and $\mathcal{N}_{Fe} = N_{init}^{(Fe)}/n_{Fe} = 27\%$ with the initial excited-state population densities $N_{init}^{(Cr),(Fe)}$ and the total ion concentrations n_{Cr} and n_{Fe}, i.e., stay below the saturation fluence of either ion species. The behavior of the singly doped and codoped sample groups is characteristically different. All samples doped with only one element, i.e., either Cr^{2+} or Fe^{2+}, exhibit a strictly single-exponential decay of PL intensity. In contrast, all codoped samples show deviations from a single-exponential decay when excited at 2.05 μm, and these deviations increase with increasing Fe^{2+} concentration (Fig. 3). This behavior is a hallmark of energy transfer from Cr^{2+} to Fe^{2+} [8,22,28].

Figure 3 summarizes normalized Cr^{2+} PL transients from all six $Fe^{2+}:Cr^{2+}:ZnSe$ codoped samples and from a singly Cr^{2+}-doped reference. The latter sample displays a PL decay time of 5.5 μs, and we estimate a Cr^{2+} quantum efficiency of approximately 85%. The inset of Fig. 3 shows the PL intensity $I_{PL}^{(Cr)}(0)$ at the maximum of the transients at $t = 0$, which exhibits a strong correlation with the number density n_{Cr} of chromium ions. While different growth methods may give rise to unsystematic deviations here, the singly Cr^{2+}-doped reference sample shows a stronger PL
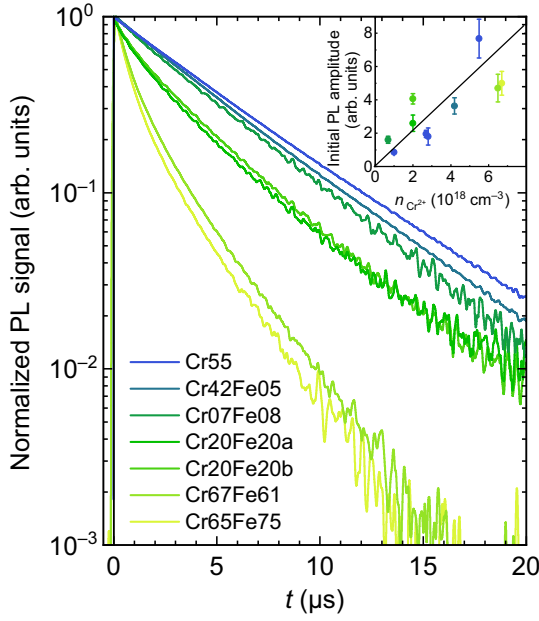
FIG. 3. Normalized PL transients from all six Fe^{2+}:Cr^{2+}:ZnSe codoped samples measured at $T = 300$ K. Excitation wavelength: 2.05 μm. Detection with the SP filter set. Shades blue through yellow indicate increasing iron concentration, with a singly Cr^{2+}-doped reference (blue on top). Cr^{2+} and Fe^{2+} concentrations are given in Table II. The inset shows the initial (peak) PL intensities for all ten samples that contain Cr^{2+} ions.

signal than the two codoped samples with higher Cr^{2+} content. Fitting a simple linear model function to the PL versus concentration dependence, we find that the Cr^{2+} reference sample lies about three standard deviations outside the fit to the codoped samples.

With the codoped samples, we perform PL measurements with direct excitation of Fe^{2+} at $\lambda_{ex} = 3.24$ μm. The Fe^{2+} PL exhibits a single-exponential decay with a time constant $\tau_{Fe} = 380$ ns [22]. Information on PL quantum yields is derived from time-integrated transients of Fe^{2+} and Cr^{2+} PL, comparing the samples Cr67Fe61 and Cr55. From the respective excitation densities $N_{init}^{(Fe), (Cr)}$ generated with the pump fluences at $\lambda_{ex} = 3.24$ μm and $\lambda_{ex} = 2.05$ μm (Table III) and for identical PL quantum yields, one would expect an approximately 7.0 times larger time-integrated PL intensity J_{PL} from the directly excited Fe^{2+} ions in the Cr67Fe61 sample than from the Cr^{2+} ions in the reference sample Cr55. The experiment, however, indicates a 2.1 times higher Cr^{2+} photon yield. Thus, the PL quantum efficiency η_{PL} of the Fe^{2+} ions is approximately 14.2 times lower than the Cr^{2+} quantum yield of 85%. Consequently, we estimate an Fe^{2+} quantum efficiency on the order of 6%. This rather small value points to pronounced nonradiative losses, which manifest themselves in the comparably short Fe^{2+} PL decay time $\tau_{PL} = 380$ ns.

TABLE III. Experimental parameters and measured quantities of the PL measurements with sample Cr67Fe61. The quantities λ_{ex} and $\hbar\omega_{ex}$ are the excitation wavelength and photon energy, while J_{ex} stands for the excitation photon flux. With the absorption cross sections σ_{abs} and the doping densities $n_{Cr,Fe}$, one derives the fraction $\mathcal{N}$ of ions excited in the impulsive limit, i.e., for excitation pulses short compared to the PL decay times. The time-integrated PL flux is given as J_{PL}, whereas τ_{PL} and η_{PL} stand for the PL decay time and quantum efficiency, respectively. The parameters μ and τ_{∞} are derived from Eq. (3).

Quantity	Cr^{2+}	Fe^{2+}
λ_{ex} (μm)	2.05	3.24
$\hbar\omega_{ex}$ (eV)	0.605	0.383
J_{ex} (10^{18} cm^{-2})	0.186	0.293
$\sigma_{abs}(\lambda_{exc})$ (10^{-18} cm^2)	0.23	0.93
$\mathcal{N} = N_{init}/n_{Cr, Fe} = J_{ex}\sigma_{abs}$	0.043	0.27
$J_{PL} = \int J_{PL}(t)dt$ (arb. units)	1	0.47
τ_{PL} (μs)	5.5	0.38
η_{PL} (%)	85	6.0
μ (meV)	⋯	230
τ_{∞} (ps)	⋯	40

The total decay rate of the emitting $^5T_2$ state (Fig. 1) of the Fe^{2+} ions can be written as [4,28,37]

$$\frac{1}{\tau} = \frac{1}{\tau_{rad}} + \frac{1}{\tau_{NR}} \approx \frac{1}{\tau_{\infty}} \exp\left(-\frac{\mu}{k_B T}\right), \qquad (3)$$

where $1/\tau_{rad}$ the radiative decay rate, $1/\tau_{NR}$ the nonradiative decay rate, k_B Boltzmann's constant, and T the sample temperature. As the radiative decay rate is more than an order of magnitude less than the overall decay rate, we neglect it in the following. The nonradiative relaxation is treated as a phonon-mediated activated process with an activation energy μ and a rate [$1/\tau_{\infty} \times \exp(-\mu/k_B T)$]. The measured decay rate $1/\tau$ is well reproduced with a time constant $\tau_{\infty} \approx 40$ ps and an activation energy $\mu = 230$ meV. The latter value is close to the activation energy [28] specified in Ref. [4] and corresponds roughly to the long-wavelength limit of the Fe^{2+} emission in Fig. 2(b). All parameter values are summarized in Table III.

Figure 4 shows time-resolved PL measurements on the codoped Fe^{2+}:Cr^{2+}:ZnSe sample Cr67Fe61 with excitation at $\lambda_{ex} = 2.05$ μm. Excitation transfer from Cr^{2+} to Fe^{2+} results in an accelerated nonexponential decay of the Cr^{2+} PL and the occurrence of Fe^{2+} PL. The kinetics of Fe^{2+} luminescence, which have been studied in more detail in Ref. [22], display a fast onset with a rise time of 60 ns and a decay on a time scale of a few microseconds. This decay is distinctly slower than after direct excitation of Fe^{2+} ($\tau = 380$ ns). Such temporal evolution is governed by excitation transfer as discussed in the next section.
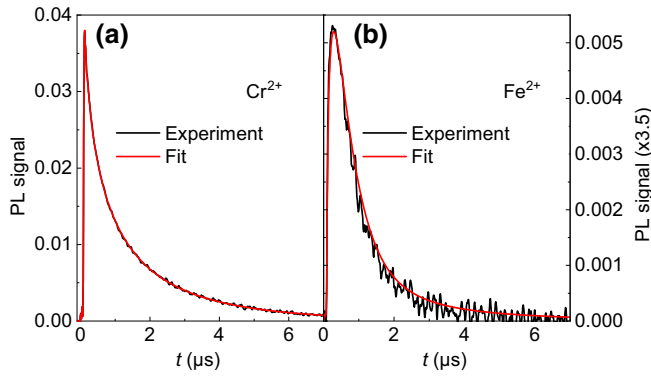
FIG. 4. PL transients taken with 2.05-μm excitation from $Fe^{2+}:Cr^{2+}$:ZnSe codoped sample Cr67Fe61 measured at $T = 300$ K with the SP (a) and LP (b) filter sets. Fits of the data are obtained using the rate equation model, i.e., Eqs. (7) and (8) for (a) and (b), respectively.
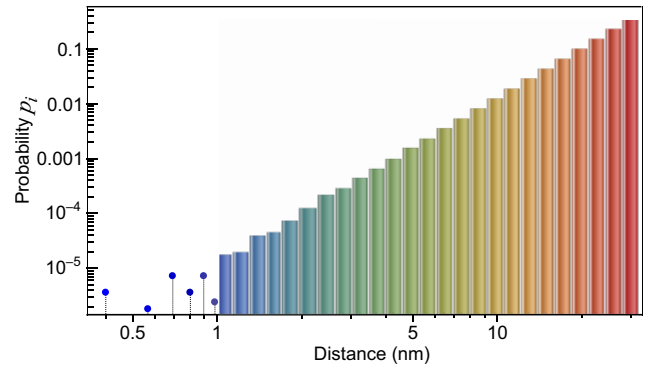

FIG. 5. Lattice statistics. As both Fe^{2+} and Cr^{2+} are known to favorably occupy Zn sites in the face-centered cubic (fcc) lattice of the ZnSe host crystal [38], only these sites have been included in the statistics. The radius is 64 unit cells. Distances up to 1 nm are included as exact numbers; distances above have been subdivided into 25 groups. Distances in each group are averaged, and probabilities are accumulated into a single number. Probabilities are normalized to unity.

V. LATTICE STATISTICS OF EXCITATION TRANSFER AND RATE EQUATION MODEL

Excitation transfer via dipole-dipole coupling of a single donor-acceptor pair is described by Eq. (1), in which the transfer time constant τ_{trans} scales with the sixth power of the distance r between a Cr^{2+} and an Fe^{2+} ion. In the codoped $Fe^{2+}:Cr^{2+}$:ZnSe samples, there is a wide distribution of donor-acceptor distances and, thus, to accurately model the PL transients, one has to sum over a large range of $Cr^{2+} - Fe^{2+}$ distances in the ZnSe lattice. If the Förster radius R_0 is large compared to the lattice constant $a = 0.566$ nm of cubic ZnSe, one can use a continuous model as an approximation that is discussed in Sec. VI. In general, however, one has to employ a discrete model, summing up transfer rates for all possible distances r_i.

The Cr^{2+} and Fe^{2+} ions mainly occupy Zn sites in the face-centered cubic lattice of ZnSe. For deriving the histogram in Fig. 5, we consider pairs of Cr^{2+} and Fe^{2+} ions with random distribution of interionic distances r_i. We then derive the r_i distribution p_i for distances between the six nearest-neighbor separations in the unit cell up to 30 nm. For 1 nm $< r_i \leq 30$ nm, the distances are arranged in 25 groups (Fig. 5) and the distribution p_i is normalized by $\sum_{i=1}^{31} p_i = 1$.

For a given distance r_i between Fe^{2+} and Cr^{2+} ions, the population $N_{Cr,i}$ then follows the rate equation:

$$\partial_t N_{Cr,i} = -[W_{Cr} + W_{DA}(r_i)] N_{Cr,i}. \quad (4)$$

Here $W_{Cr} = 1/\tau_{Cr}$ accounts for the PL decay in the absence of excitation transfer and $W_{DA}(r_i) = \alpha_{DA} r_i^{-6}$ is the transfer rate from donor to acceptor at distance r_i. Any back transfer from Fe^{2+} to Cr^{2+} ions is neglected, as is transfer between Cr^{2+} ions. Equation (4) is readily solved to yield

$$N_{Cr,i}(t) = p_i \exp\left(- [W_{Cr} + W_{DA}(r_i)] t\right). \quad (5)$$

This solution can then be plugged into the respective equation for the Fe^{2+} ions

$$\partial_t N_{Fe} = -W_{Fe} N_{Fe} + \sum_{i=1}^{31} W_{DA}(r_i) N_{Cr,i}. \quad (6)$$

The time-dependent PL signals are then given by

$$P_{Cr}(t) = \exp\left(-W_{Cr}t\right) \sum_{i=1}^{31} p_i \exp\left[-W_{DA}(r_i)t\right], \quad (7)$$

$$P_{Fe}(t) = \sum_{i=1}^{31} \frac{p_i W_{DA}(r_i)}{W_{DA}(r_i) + W_{Cr} - W_{Fe}} \left[\exp\left(-W_{Fe}t\right) - \exp\left(-\frac{W_{Fe}\left[W_{Cr} + W_{DA}(r_i)\right]}{W_{Cr}} t\right) \right]. \quad (8)$$

This result allows for determining the coefficient α_{DA} from the measured Cr^{2+} PL transients by separating the emission decay W_{Cr} of the Cr^{2+} ions from the excitation transfer process to Fe^{2+} ions (Fig. 4). Fitting Eq. (7) to the measured Cr^{2+} PL, we determine $\alpha_{DA} = 330$ nm^6/μs and a Förster radius $R_0 = \sqrt[6]{\alpha \tau_{Cr}} = 3.5$ nm. Such numbers indicate that excitation transfer rates are about 3.7 times higher than expected from Förster theory of resonant energy transfer [Eq. (1)].

The enhanced transfer rates are additionally verified by comparing the measured Fe^{2+} PL signal with the one expected for such a fast transfer process, allowing only for an adaption of the amplitude. As shown in Fig. 4(b), this approach provides an excellent fit to the data, confirming the rapid transfer process. Analyzing the contributions

from different distances r_i, one finds that the rapid buildup time of the Fe^{2+} PL of 60 ns [22] originates from Cr^{2+} ions at distances below 2 nm, i.e., $r_i \leq R_0/2$. The Fe^{2+} PL signal peaks at about 150 ns after the initial Cr^{2+} excitation. Subsequently, fluorescent and nonradiative decay processes start to surpass the transfer process, and the Fe^{2+} PL decays on an extended time scale of several microseconds, much slower than the 380-ns decay observed after resonant excitation of Fe^{2+} ions. The extension of the decay of Fe^{2+} PL is due to excitation transfer from Cr^{2+} ions at later times, corresponding to larger distances r_i up to approximately equal to $20a$. This picture is supported by the nonexponential decay of Cr^{2+} PL (Fig. 3) with a fast depletion within the first few microseconds and a slower decay at longer times.

VI. CONTINUUM MODEL AND TRANSFER EFFICIENCIES

Having discussed the sample with the highest available doping level in the rather elaborate discrete rate-equation model, we conclude that the Förster radius is always at least an order of magnitude larger than the lattice constant. Further restricting ourselves to dipole-dipole interaction in the transfer process, one can use a continuum model for the donor fluorescence [28,39]

$$P_D(t) = P_0 \exp\left[-\frac{t}{\tau_{Cr}} - \gamma\sqrt{t}\right], \qquad (9)$$

where the slope γ of the nonexponential contribution from the transfer process is related to α_{DA} via the relation

$$\alpha_{DA} = \frac{9\gamma^2}{16n_{Fe}^2\pi^3}, \qquad (10)$$

(cf. Table I). Using a singly Cr^{2+}-doped reference sample with $n_{Fe} \ll 3 \times 10^{16}$ cm^{-3} for determining τ_{Cr}, we can now readily determine the slope γ for the different codoped samples by plotting the normalized PL transients in Fig. 3 as

$$\Gamma(\sqrt{t}) = \ln\left(\frac{P_{ref}(t)}{P_{ref}(0)}\right) - \ln\left(\frac{P_D(t)}{P_D(0)}\right) \qquad (11)$$

and fitting the relationship $\Gamma(\sqrt{t}) = \gamma\sqrt{t}$ to the renormalized transients [Fig. 6(a)]. As shown in Fig. 6(b), the slope γ in this representation scales linearly with iron concentration, reaching values above 1000 $\sqrt{s^{-1}}$ for the samples with highest Fe^{2+}-doping levels available. We also verify the dipole-dipole character of the interaction by fitting a generalization of Eq. (9) [28] to the data in Fig. 4(a). With Eq. (10) one can now determine the average value $\alpha_{DA} = 435 \pm 60$ nm^6/µs, which is much higher than the theoretical estimate $\alpha_{DA} = 90$ nm^6/µs from the
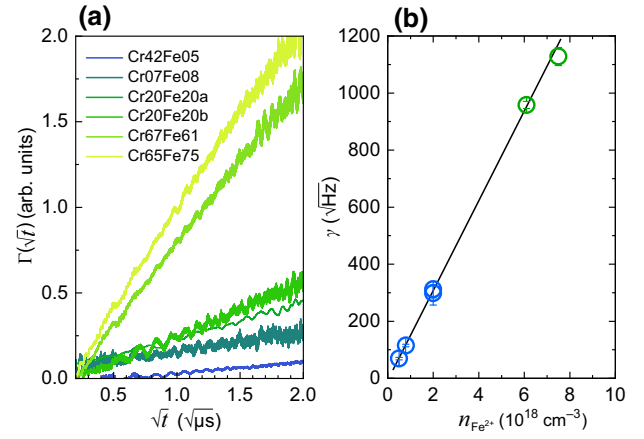

FIG. 6. (a) PL decays displayed in Fig. 3 after subtraction of the contribution of the exponential fraction of the recombination according to Eq. (11) [9]. (b) Slopes as determined from (a) in the 0.5 to 1.5-$\sqrt{\mu s}$ range versus iron ion concentration for all codoped samples. Blue symbols: single-crystalline ZnSe. Green symbols: polycrystalline ZnSe.

elementary Förster approach (cf. Table I). Consequently, statistical analysis of Fig. 6 indicates an acceleration of the transfer by a factor 4.8 ± 0.7, which agrees within 1.5 standard deviations with the value extracted from the rate-equation analysis on the sample Cr67Fe61 [Fig. 4]. This acceleration can be explained by accounting for additional (multi)phonon-assisted excitation transfer [40] via

$$\gamma^2(T) = \gamma_0^2 \left(\frac{1}{\exp(\hbar\omega_{LO}/k_B T) - 1} + 1\right)^{\overline{\nu}}, \qquad (12)$$

where $\hbar\omega_{LO} = 31$ meV is the LO-phonon energy and $\overline{\nu} = 4.5$ is the average phonon number. Assuming a Fe^{2+} doping level of 6×10^{18} cm^{-3}, letting $\gamma_0 = 420\sqrt{s^{-1}}$ is found to match our experimentally observed acceleration of the excitation transfer. Finally, using the experimental value $\alpha_{DA} = 435$ nm^6/µs, one deduces a Förster radius $R_0 = 3.65 \pm 0.08$ nm and critical Fe^{2+} doping density $n_0 = (4.9 \pm 0.3) \times 10^{18}$ cm^{-3}.

The enhanced energy-transfer rates translate in a high transfer efficiency η_{DA}, which is given by [9]

$$\eta_{DA} = \frac{\gamma^2}{\gamma^2 + \tau_{Cr}^{-1}}, \qquad (13)$$

and, alternatively,

$$\eta_{DA} = 1 - \frac{\int_0^\infty P_D(t)/P_D(0)dt}{\int_0^\infty P_{ref}(t)/P_{ref}(0)dt}. \qquad (14)$$

Figure 7 shows transfer efficiencies η_{DA} calculated from Eqs. (13) and (14) as a function of the Fe^{2+} acceptor density n_{Fe}. With the exception of low doping levels $n_{Fe} <$
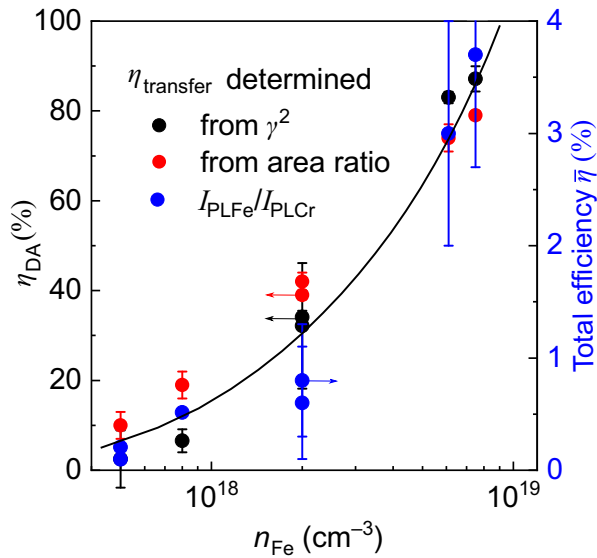
FIG. 7. $Cr^{2+} \rightarrow Fe^{2+}$ excitation transfer efficiency (η_{DA}) calculated from the γ^2 presented in Fig. 6 via Eq. (13) [full black circles]. Alternatively η_{DA} is determined from the area ratios of the transients displayed in Fig. 4 via Eq. (14) [full red circles]. The right ordinate shows the integrated PL intensity ratios of Fe^{2+} to Cr^{2+} PLs for the same samples, yielding the total efficiencies $\overline{\eta}$ [full blue circles]. The line is a guide to the eye.

10^{18} cm^{-3}, the values obtained by either method agree within 10%, with $\eta_{DA} > 50\%$ for $n_{Fe} > n_0$. For the highest available doping level $n_{Fe} = 7.5 \times 10^{18}$ cm^{-3}, the transfer efficiency exceeds 80%.

The results of our PL measurements (cf. Fig. 4) allow for benchmarking the transfer efficiencies derived from Eqs. (13) and (14). Blue symbols in Fig. (7) indicate the ratio of the time-integrated PL signals from Fe^{2+} and Cr^{2+}, i.e., the total efficiency $\overline{\eta}$, which reaches a maximum value of some 4% at the highest Fe^{2+} concentration. $\overline{\eta}$ is given by the product of the transfer efficiency η_{DA} and the Fe^{2+} PL quantum yield. Using the η_{DA} values from Eqs. (13) and (14) and the Fe^{2+} PL quantum yield of approximately 5%, the PL area ratios are well reproduced within the experimental accuracy. This analysis shows that the Fe^{2+} PL quantum yield and not the efficiency of excitation transfer limits utility of this material system for laser applications in the midinfrared.

VII. DISCUSSION

Our detailed analysis of excitation-transfer processes in Cr^{2+} and Fe^{2+} (co)doped ZnSe at $T = 300$ K demonstrates excitation-transfer rates and transfer efficiencies that are substantially higher than anticipated from the elementary Förster picture of resonant energy transfer. The transfer efficiency reaches values around 80% at doping levels of 6×10^{18} cm^{-3}. The accelerated excitation

transfer from $Cr^{2+} \rightarrow Fe^{2+}$ manifests itself in a pronounced nonexponential decay of Cr^{2+} PL, characteristic for electronic excitation transfer via dipole-dipole coupling.

The Fe^{2+} ions in ZnSe display a pronounced coupling to phonons. Jahn-Teller coupling to acoustic phonons at frequencies below 12.5 meV and transverse optical phonons around 26 meV has a direct impact on the low-temperature absorption spectra of Fe^{2+} [41]. Moreover, the efficient radiationless decay of the Fe^{2+} ${}^5T_2$ excited state has been assigned to a thermally activated decay mechanism [Eq. (3)], involving strong electron-phonon coupling [4]. In a similar way, the $Cr^{2+} - Fe^{2+}$ excitation transfer is expected to be enhanced by phonon-assisted contributions, which compensate for the mismatch of the electronic transition energies between the Cr^{2+} donor and Fe^{2+} acceptor ions. In other words, on top of the electronically resonant transfer described by Eq. (1), there are phonon-mediated processes that enhance the effective overlap between donor emission and acceptor absorption.

Phonon-assisted transfer rates have been analyzed in the seminal Ref. [42] and are related directly to phonon-mediated radiationless decay rates. For multi-phonon excitation transfer, the electronic dipole-dipole coupling matrix element, the electron-phonon coupling strength, and the overlap of multiphonon donor emission and acceptor absorption lines are the rate-determining quantities. At $T = 300$ K with substantial thermal phonon populations, stimulated phonon emission enhances the excitation transfer rates [40,42]. While a quantitative calculation of the transfer rates is beyond the scope of the present work, we emphasize that the substantial spectral width of the Cr^{2+} emission and Fe^{2+} absorption spectrum favors the parallel occurrence of a multitude of phonon-assisted transfer channels. It is interesting to note that the enhancement of the excitation transfer rates by a factor of approximately equal to 5 [compared to the elementary Förster picture Eq. (1)] results in an overall rate close to what Eq. (1) predicts for a perfect overlap of the Cr^{2+} emission and Fe^{2+} absorption spectrum.

Apart from phonon-assisted excitation transfer, it is conceivable that other mechanisms may have contributed to the observed acceleration. In particular, as excitation transfer processes scale with $\langle n_0^2 \rangle$ and absorption with $\langle n_0 \rangle$, inhomogeneous doping ($\langle n_0^2 \rangle \neq \langle n_0 \rangle^2$) or clustering effects could contribute to the observed enhancement of transfer rates. Nevertheless, in order to explain an acceleration by a factor of 5, doping levels must vary by more than an order of magnitude, e.g., between a highly doped but narrow surface layer and an effectively undoped and much thicker core layer. Given that we include both polycrystalline and single-crystal samples in our study, we expect that diffusion of the active ions results in strong variations of the homogeneity of the doping, that is, singly crystal samples [green symbols in Fig. 6] should show different

acceleration than polycrystalline ones [blue symbols in Fig. 6]. Inspecting Fig. 6(b), however, no such trend appears. We thus rule out doping inhomogeneities as a key mechanism of enhancement. Doping inhomogeneities may nevertheless explain small discrepancies seen in some of the data, e.g., different values of γ at identical doping levels.

A third rationale for explaining temperature variations of the transfer efficiency is given by the overlap integral $\int g_D(E)g_A(E)dE$ in Eq. (1), which is expected to vary by a factor 2 between room and liquid-nitrogen temperatures. Yet, all pertinent measurements that went into estimation of the overlap integral are done at room temperatures. So, this explanation can also be ruled out for explaining the efficiency increase and acceleration of the excitation transfer in $Fe^{2+}:Cr^{2+}:ZnSe$.

While it now appears straightforward to achieve high transfer efficiencies, the remaining problem is the rather large nonradiative loss of the Fe^{2+} ions at room temperature. We therefore observe only a total luminous efficiency $\overline{\eta}$ below 5%, despite a high transfer efficiency η_{DA}. As both processes are ruled by a similar temperature dependence, it may therefore appear questionable whether one can decrease nonradiative losses of the Fe^{2+} ions without also decreasing the transfer efficiency. Combining Eqs. (12) and (13), we yield an expression for the total efficiency

$$\overline{\eta}(T) = \frac{\gamma^2(T)}{\gamma^2(T) + \tau_{Cr}^{-1}} \frac{\tau_{Cr}^{-1}}{\tau_{Cr}^{-1} + \tau_{Fe}^{-1}(T)}. \quad (15)$$

The second factor in Eq. (15) describes nonradiative losses of the Fe^{2+} ions. At low temperatures $\tau_{Fe} \gg \tau_{Cr}$, so this factor converges to unity. Conversely if $\tau_{Fe} \ll \tau_{Cr}$, the efficiency is degraded by the ratio τ_{Fe}/τ_{Cr}. Resulting temperature dependencies $\overline{\eta}(T)$ for different doping concentrations n_{Fe} are shown in Fig. 8. Assuming the highest Fe^{2+} concentrations available in this study, we estimate that the overall efficiency $\overline{\eta}$ increases by a factor 10 to $> 40\%$ at temperatures of 200 K. The dashed curves in Fig. 8 show that the transfer efficiency degradation amount to only about 25% whereas the fluorescent lifetime increases from 380 ns at ambient to > 20 μs below 200 K. If higher doping concentrations $n_{Fe} > 10^{19}$ cm^{-3} become available, overall efficiencies near 80% appear possible over a wide cryogenic temperature range.

VIII. CONCLUSIONS

Our experimental study reveals room-temperature rates of electronic excitation transfer in $Fe^{2+}:Cr^{2+}:ZnSe$ that are about 5 times higher than expected from elementary Förster transfer theory. Such rates enhance the transfer efficiency strongly. This enhancement is assigned to a
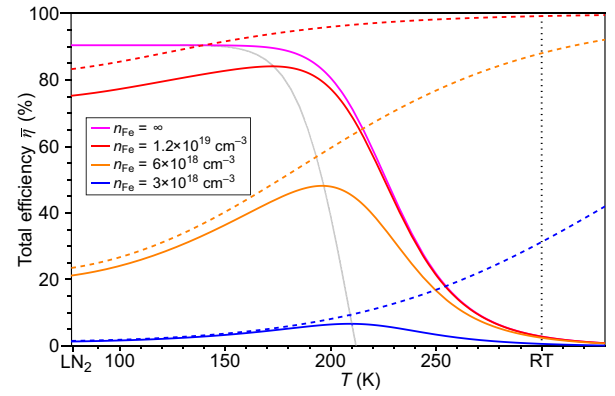

FIG. 8. Efficiency versus temperature according to Eq. (15). LN$_2$, liquid nitrogen temperature; RT, room temperature. Dashed curves: Förster transfer efficiencies η_{DA}. Solid curves: overall efficiencies $\overline{\eta}$ accounting for both increasing nonradiative losses of the Fe^{2+} ions with increasing temperature and Förster transfer efficiencies. Solid gray curve: predicted "sweet spot" of maximum overall efficiency $\overline{\eta}$ for a range of Fe^{2+} concentrations. Dotted black line: room-temperature conditions present in our experiments. Violet curve: projected efficiency at infinite iron concentration. Red curves: efficiency at maximum beneficial concentration imposed by quenching effects. Orange curve: maximum Fe^{2+} concentration available in our study. Blue curves: efficiencies for one of the samples with lower Fe^{2+} content.

prominent contribution of (multi)phonon-assisted excitation transfer to the overall transfer rates. In our room-temperature experiments, maximum transfer efficiencies above 80% are observed for Fe^{2+}-doping densities in the range of 6×10^{18} cm^{-1}. Given that multiphonon processes also greatly increase nonradiative losses of excited Fe^{2+} ions, we nevertheless observe only rather poor overall photoluminescence efficiency below 5%. Previously, researchers tried to mitigate this problem by using higher doping levels, which, however, cannot be arbitrarily increased because of, e.g., concentration-quenching effects. Given the above considerations, the key to efficient exploitation of the Förster transfer process does not appear a further increase of doping concentrations, but operation of $Fe^{2+}:Cr^{2+}:ZnSe$ in the range from $-80\,°C$ to $-100\,°C$. In this temperature range, nonradiative losses of the Fe^{2+} ions appear sufficiently suppressed, and the transfer efficiency reduces by only 10% to 20% compared to room temperature, such that overall efficiencies above 50% appear feasible with careful temperature control. Considering also higher doping levels than are available in our study, we believe that overall efficiencies larger than 80% may be possible. In closing, we believe that our findings open up an alternative avenue for efficient use of the $Fe^{2+}:Cr^{2+}:ZnSe$ material system, offering broadband laser action and amplification in the 4-5 μm wavelength range using commercially available pump sources in the 2-μm wavelength range.

ACKNOWLEDGMENTS

---

[1] E. A. Migal, S. S. Balabanov, D. V. Savin, V. B. Ikonnikov, E. M. Gavrishchuk, and F. V. Potemkin, Amplification properties of polycrystalline Fe:ZnSe crystals for high power femtosecond mid-IR laser systems, Opt. Mater. **111,** 110640 (2021).

[2] E. A. Migal, A. Pushkin, B. Bravy, V. Gordienko, N. Minaev, A. Sirotkin, and F. Potemkin, 3.5-mJ 150-fs Fe:ZnSe hybrid mid-IR femtosecond laser at 4.4 μm for driving extreme nonlinear optics, Opt. Lett. **44,** 2250 (2019).

[3] V. Y. Ivanov, M. Godlewski, A. Szczerbakow, A. Omel'Chuk, A. Davydov, N. Zhavoronkov, and G. Raciukaitis, Optically pumped mid-infrared stimulated emission of ZnSe:Cr crystals, Acta Phys. Pol. A **105,** 553 (2004).

[4] V. V. Fedorov, S. B. Mirov, A. Gallian, D. V. Badikov, M. P. Frolov, Y. V. Korostelin, V. I. Kozlovsky, A. I. Landman, Y. P. Podmar'kov, V. A. Akimov, and A. A. Voronov, $3.77 - 5.05$-μm tunable solid-state lasers based on Fe^{2+}-doped ZnSe crystals operating at low and room temperatures, IEEE J. Quantum Electron. **42,** 907 (2006).

[5] IPG Photonics - Southeast Technology Center, Mid-Infrared Lasers, Birmingham, AL, https://www.ipgphotonics.com/en/products/lasers/mid-ir-hybrid-lasers.

[6] M. E. Doroshenko, H. Jelínková, P. Koranda, J. Šulc, T. T. Basiev, V. V. Osiko, V. K. Komar, A. S. Gerasimenko, V. M. Puzikov, V. V. Badikov, and D. V. Badikov, Tunable mid-infrared laser properties of Cr^{2+}:ZnMgSe and Fe^{2+}:ZnSe crystals, Laser Phys. Lett. **7,** 38 (2010).

[7] M. E. Doroshenko, V. V. Osiko, H. Jelínková, M. Jelínek, J. Šulc, M. Němec, D. Vyhlídal, M. Čech, N. O. Kovalenko, and A. S. Gerasimenko, Spectroscopic and laser properties of bulk iron doped zinc magnesium selenide Fe:ZnMgSe generating at $4.5 - 5.1$ μm, Opt. Express **24,** 19824 (2016).

[8] M. Doroshenko, M. Jelínek, A. Říha, J. Šulc, H. Jelínková, V. Kubeček, N. O. Kovalenko, and A. S. Gerasimenko, Long-pulse $4.4 - 4.6$ μm laser oscillations of Fe^{2+} ions in a $Zn_{1-x}Mn_xSe$ ($x = 0.3$) crystal pumped by a 1940 nm Tm

fiber laser through $Cr^{2+} \rightarrow Fe^{2+}$ energy transfer, Opt. Lett. **44,** 5334 (2019).

[9] M. E. Doroshenko, H. Jelínková, A. Říha, M. Jelínek, M. Němec, N. O. Kovalenko, and A. S. Gerasimenko, Mid-IR (4.4 μm) $Zn_{1-x}Mn_xSe:Cr^{2+}$, Fe^{2+} ($x = 0.3$) laser pumped by 1.7 μm laser using $Cr^{2+} \rightarrow Fe^{2+}$ energy transfer, Opt. Lett. **44,** 2724 (2019).

[10] A. Říha, H. Jelínková, M. E. Doroshenko, M. Jelínek, J. Šulc, M. Němec, M. Čech, D. Vyhlídal, and N. O. Kovalenko, Gain-switched laser operation of Cr^{2+},Fe^{2+}:$Zn_{1-x}Mg_xSe$ ($x \approx 0.2; x \approx 0.3$) single crystals under $Cr^{2+} \rightarrow Fe^{2+}$ energy transfer at ~ 1.73 μm and direct Fe^{2+} ions excitation at ~ 2.94 μm, J. Lumin. **240,** 118375 (2021).

[11] M. E. Doroshenko, V. V. Osiko, H. Jelínková, M. Jelínek, N. O. Kovalenko, and I. S. Terzin, $Cd_{1-x}Mn_xTe$ ($x = 0.1 - 0.78$) crystals doped with Fe^{2+} ions: Spectroscopic properties and laser oscillations at 4.95–5.27 μm at low temperature, Laser Phys. Lett. **14,** 025801 (2017).

[12] M. E. Doroshenko, V. V. Osiko, H. Jelínková, M. Jelínek, J. Šulc, D. Vyhlídal, N. O. Kovalenko, and I. S. Terzin, Spectral and lasing characteristics of Fe:$Cd_{1-x}Mn_xTe$ ($x = 0.1 - 0.76$) crystals in the temperature range 77 to 300 K, Opt. Mater. Express **8,** 1708 (2018).

[13] J. W. Evans, B. D. Dolasinski, T. R. Harris, J. W. Cleary, and P. A. Berry, Demonstration and power scaling of an Fe:CdMnTe laser at 5.2 microns, Opt. Mater. Express **7,** 860 (2017).

[14] T. P. Surkova, P. Kaczor, A. J. Zakrzewski, K. Swiatek, V. Y. Ivanov, M. Godlewski, A. Polimeni, L. Eaves, and W. Giriat, Optical properties of ZnSe, ZnCdSe and ZnSSe alloys doped with iron, J. Cryst. Growth **214,** 576 (2000).

[15] J. Peppers, V. V. Fedorov, and S. B. Mirov, Mid-IR photoluminescence of Fe^{2+} and Cr^{2+} ions in ZnSe crystal under excitation in charge transfer bands, Opt. Express **23,** 4406 (2015).

[16] V. Fedorov, T. Carlson, and S. Mirov, Energy transfer in iron-chromium co-doped ZnSe middle-infrared laser crystals, Opt. Mater. Express **9,** 2340 (2019).

[17] T. Carlson, O. Gafarov, V. Fedorov, and S. Mirov, in *Laser Congress 2018 (ASSL)*, OSA Technical Digest (Optical Society of America, 2018), p. AW3A.7.

[18] A. A. Lagatsky, F. Fusari, S. V. Kurilchik, V. E. Kisel, A. S. Yasukevich, N. V. Kuleshov, A. A. Pavlyuk, C. T. A. Brown, and W. Sibbett, Optical spectroscopy and efficient continuous-wave operation near 2 μm for a Tm,Ho:KYW laser crystal, Appl. Phys. B **97,** 321 (2009).

[19] V. Jambunathan, A. Schmidt, X. Mateos, M. C. Pujol, U. Griebner, V. Petrov, C. Zaldo, M. Aguilo, and F. Diaz, Crystal growth, optical spectroscopy, and continuous-wave laser operation of co-doped (Ho,Tm):$KLu(WO_4)_2$ monoclinic crystals, J. Opt. Soc. Am. B **31,** 1415 (2014).

[20] X. Wang, Z. Chen, L. Zhang, B. Jiang, M. Xu, J. Hong, Y. Wang, P. Zhang, L. Zhang, and Y. Hang, Preparation, spectroscopic characterization and energy transfer investigation of iron-chromium diffusion co-doped ZnSe for mid-IR laser applications, Opt. Mater. **54,** 234 (2016).

[21] V. A. Antonov, K. N. Firsov, E. M. Gavrishchuk, V. B. Ikonnikov, I. G. Kononov, T. V. Kotereva, S. V. Kurashkin, S. V. Podlesnykh, S. A. Rodin, D. V. Savin, A. A. Sirotkin,

A. M. Titirenko, and N. V. Zhavoronkov, Luminescent and lasing characteristics of polycrystalline Cr:Fe:ZnSe exited at 2.09 and 2.94 µm wavelengths, Laser Phys. Lett. **16,** 095002 (2019).

[22] P. Fuertjes, J. W. Tomm, U. Griebner, S. S. Balabanov, E. M. Gavrishchuk, and T. Elsaesser, Kinetics of excitation transfer from Cr^{2+} to Fe^{2+} ions in co-doped ZnSe, Opt. Lett. **47,** 2129 (2022).

[23] G. Grebe, G. Roussos, and H.-J. Schulz, Cr^{2+} excitation levels in ZnSe and ZnS, J. Phys. C **9,** 4511 (1976).

[24] S. S. Mitra, Phonon assignments in ZnSe and GaSb and some regularities in the phonon frequencies of zincblende-type semiconductors, Phys. Rev. **132,** 986 (1963).

[25] E. Sorokin, S. Naumov, and I. Sorokina, Ultrabroadband infrared solid-state lasers, IEEE J. Sel. Top. Quantum Electron. **11,** 690 (2005).

[26] T. Förster, Experimentelle und theoretische Untersuchung des zwischenmolekularen Übergangs von Elektronenanregungsenergie, Z. Naturforsch. A **4,** 321 (1949).

[27] D. Dexter, A theory of sensitized luminescence in solids, J. Chem. Phys. **21,** 836 (1953).

[28] B. Henderson and M. Imbusch, *Optical Spectroscopy of Inorganic Solids (Monographs on the Physics And Chemistry of Materials, Vol. 44)* (Oxford Science Publications, Oxford, 2006).

[29] D. Marple, Refractive index of ZnSe, ZnTe, and CdTe, J. Appl. Phys. **35,** 539 (1964).

[30] J. Kernal, V. Fedorov, A. Gallian, S. Mirov, and V. Badikov, $3.9 - 4.8$ µm gain-switched lasing of Fe:ZnSe at room temperature, Opt. Express **13,** 10608 (2005).

[31] I. T. Sorokina and E. Sorokin, Femtosecond Cr^{2+}-based lasers, IEEE J. Sel. Top. Quantum Electron. **21,** 1601519 (2014).

[32] E. M. Gavrishchuk, V. B. Ikonnikov, and S. S. Balabanov, Patent RU2549419C1, Production of alloyed zinc chalcogenides and their solid solutions, priority date 26.12.2013 (2013).

[33] S. B. Mirov, V. V. Fedorov, D. Martyshkin, I. S. Moskalev, M. Mirov, and S. Vasilyev, Progress in Mid-IR lasers based on Cr and Fe-Doped II-VI chalcogenides, IEEE J. Sel. Top. Quantum Electron. **21,** 1601719 (2015).

[34] J. W. Evans, T. R. Harris, B. R. Reddy, K. L. Schepler, and P. A. Berry, Optical spectroscopy and modeling of Fe^{2+} ions in zinc selenide, J. Lumin. **188,** 541 (2017).

[35] J. M. Baranowski, J. W. Allen, and G. L. Pearson, Crystal-field spectra of $3d^n$ impurities in II-VI and III-V compound semiconductors, Phys. Rev. **160,** 627 (1967).

[36] P. Fuertjes, L. von Grafenstein, D. Ueberschaer, C. Mei, U. Griebner, and T. Elsaesser, Compact OPCPA system seeded by a Cr:ZnS laser for generating tunable femtosecond pulses in the MWIR, Opt. Lett. **46,** 1704 (2021).

[37] N. Myoung, V. V. Fedorov, S. B. Mirov, and L. E. Wenger, and Temperature and concentration quenching of mid-IR photoluminescence in iron doped ZnSe and ZnS laser crystals, J. Lumin. **132,** 600 (2012).

[38] Simple crystal structure and Miller indices, Wolfram demonstrations project, https://demonstrations.wolfram.com/simplecrystalstructuresandmillerindices/.

[39] M. Inokuti and F. Hirayama, Influence of energy transfer by the exchange mechanism on donor luminescence, J. Chem. Phys. **43,** 1978 (1965).

[40] N. Yamada, S. Shionoya, and T. Kushida, Phonon-assisted energy transfer between trivalent rare earth ions, J. Phys. Soc. Jpn. **32,** 1577 (1972).

[41] O. Mualin, E. E. Vogel, M. A. de Orúe, L. Martinelli, G. Bevilacqua, and H. J. Schulz, Two-mode Jahn-Teller effect in the absorption spectra of Fe^{2+} in II-VI and III-V semiconductors, Phys. Rev. B **65,** 035211 (2001).

[42] T. Miyazawa and D. L. Dexter, Phonon sidebands, multiphonon relaxation of excited states, and phonon-assisted energy transfer between ions in solids, Phys. Rev. B **1,** 2961 (1970).